PROCEEDINGS, 41st Workshop on Geothermal Reservoir Engineering
Stanford University, Stanford, California, February 22-24, 2016
SGP-TR-209

Sheet Silicate Dissolution at Elevated Temperature: A Comparison of Dissolution Kinetics of Chlorite, Illite, and Biotite

Megan M. Smith and Susan A, Carroll

Atmospheric, Earth, & Energy Division; Lawrence Livermore National Laboratory; Livermore, CA 94609 USA

megan@llnl.gov; carroll6@llnl.gov

Keywords: geothermal, geochemistry, sheet silicate, chlorite, illite, biotite, phyllosilicate, kinetics, boehmite, precipitation, clay

ABSTRACT

Sheet silicates are important and abundant minerals in hydrothermal systems, making up significant portions of solid-phase volume in some geothermal reservoirs. The reactivity of these sheet silicates is of special interest when these minerals occur within naturally occurring geothermal fractures or in adjoining wallrock, where large volumes of out-of-equilibrium fluids cycle through the geothermal system. We have identified a lack of kinetic data for many sheet silicates at temperatures above 100 °C, and have been conducting kinetic dissolution experiments to close this data gap for three specific minerals: chlorite (Mg-Al-silicate), illite (K-Al-silicate), and biotite (K-Mg-Al-silicate). Experiments were conducted over 100-280 °C and a pH range of 3-9, and the resulting rates were combined with pre-existing lower-temperature data (where available) to produce kinetic rate equations applicable at (sub-280 °C) geothermal temperatures. Specifically, we find that previously published rate equations from 25 °C data both over- (in the case of chlorite) and underpredict (in the case of illite) rates at higher-temperature geothermal conditions. Our experiments show that illite is the most reactive of the three sheet silicates, with rates increasing by over 1000 times from 100-280 °C at a given pH over a 3-4 day timescale, compared to only a 10-50fold increase in chlorite and biotite rates at the same conditions. We find that illite dissolution under acid conditions is accompanied by rapid co-precipitation of aluminum oxy-hydroxide solids, with no secondary precipitation noted under neutral or alkaline conditions. In comparison, chlorite and biotite experiments showed no evidence of secondary precipitates, and rates showed little variability with pH $\geq$ 5 as solutions approached equilibrium with magnesium-hydroxide phases. We present kinetic rate equations that should be helpful for better prediction of the long-potential term impacts of geochemical alteration on reservoir permeability.

1. INTRODUCTION

The reactivity of minerals present in naturally fractured zones in geothermal reservoirs is of interest because these regions often preferentially transmit large volumes of fluid during geothermal operations, or they may be targeted for subsurface stimulation to further enhance reservoir permeability (enhanced or engineered geothermal systems, EGS). If increased permeability can be achieved, this means that greater volumes of heat-transfer fluids can be cycled through the system. Injected fluids are likely to be in chemical and thermal disequilibrium with the host rock, increasing the likelihood of fluid-mineral reactivity. The effect of mineral reactivity on fracture walls, fracture asperities, and fracture-matrix interaction is currently difficult to predict. Reactive fracture flow studies in a variety of rock types have shown a range of responses to increased reactivity, from increased flow due to widening of average fracture apertures, the development of fast flowpaths or channels associated with fractures, enhanced wallrock porosity and diffusive transport into the matrix, as well as permeability decreases due to the dissolution of fracture-propping asperities (e.g., Smith et al., 2014; Ellis et al., 2013; Smith et al., 2013; Yasuhara et al., 2006; Yasuhara and Elsworth, 2004; Polak et al., 2004; Detwiler et al., 2003; Polak et al., 2003; Durham et al., 2001; Moore et al., 1994). Likely the overall impact to reservoir sustainability will depend upon a combination of geochemical and geomechanical factors. However, our current ability to confidently predict geochemical effects on flow and transport is hampered by a lack of kinetic data for mineral reactivity at the higher (100°C+) temperatures relevant to geothermal operations.

The majority of higher-temperature kinetic rates have been collected from experiments on quartz and feldspars, which together comprise a large percentage of the mineral volume in a typical geothermal reservoir. For the majority of all other minerals, however, available kinetic data have been collected primarily at 25°C and are rare even above 80°C (e.g., Palandri and Kharaka, 2004). Sheet silicates, including clays and mica minerals, can make up a significant percentage of mineral volume in hydrothermal fracture zones (e.g., Lutz et al., 2010). Despite their common occurrence in geothermal systems, few studies have focused on the kinetics of sheet silicate dissolution at geothermal temperatures.

We have conducted a series of experiments, covering a pH range of 3-9 and temperatures of 100-280°C, with the objective of filling the data gap for kinetic dissolution rates of some important sheet silicates. These rates are used to derive useful kinetic rate equations for use in reactive transport simulations of geothermal systems. Chlorite (Mg-(Fe)-Al-silicate), illite (K-Al-silicate), and biotite (K-Mg-(Fe)-silicate) were selected for study. We focus on results from the most recently studied mineral, biotite, and compare the trends in biotite dissolution rates to those observed previously for chlorite and illite.

2. MATERIALS AND METHODS

Over 80 kinetic dissolution experiments have been conducted using minerals obtained from the Clay Mineral Repository and from other research groups. Characterization and analysis techniques and experimental methods are similar among the three studies and details are given below.

2.1 Mineral characterization

These sheet silicates consist of repeating sequences of sheets of tetrahedrally and octahedrally coordinated cations (T-O-T layers). Differing cation substitutions within the layers in biotite and illite require some amount of interlayer cations (potassium, sodium, etc.) to balance charge within the structure; in the case of chlorite, an additional brucite-like octahedral layer instead repeats between T-O-T layers. All mineral solids were crushed by ball milling and mechanically sieved to retain the 150-250 μm size fractions. All minerals were used as received with the exception of the illite. Unreacted and reacted mineral solids were characterized by a variety of methods, including X-ray diffraction (XRD), electron microprobe compositional measurements, scanning and transmission electron microscopy imaging (SEM, TEM), and N_2-BET surface area measurements.

2.1.1 Chlorite

An Mg-rich (clinochlore) variety from Flagstaff Hills, California, USA, was procured from the Clay Minerals Society and prepared for dissolution reaction. Isolated rutile grains were noted with SEM imaging. The composition of the chlorite was determined by electron microprobe analyses to be $(Mg_{4.29}Al_{1.48}Fe_{0.10})(Al_{1.22}Si_{2.78})O_{10}(OH)_8$, and the 150-250 μm size fraction had a specific surface area of 4.9 ±0.3 m^2 g^{-1}. Dissolution at acid conditions did not affect the measured specific surface area, while neutral and alkaline dissolution showed only slight decreases (1-3x lower) in surface area as a result of reaction. SEM imaging using electron dispersive spectrometry (EDS) and TEM analysis and diffractometry found no evidence of secondary mineral precipitates in chlorite grains reacted over the full range of temperatures and pH conditions. More details are provided in Smith et al. (2013) and Smith and Carroll (2016).

2.1.2 Illite

Large masses of illite from Silver Hill, Montana, USA, were purchased from the Clay Minerals Society and disaggregated before a weak acid pre-treatment (e.g., Zavarin et al., 2012) to remove reported carbonate impurities, and then sieved. The composition of the illite was determined to be $K_{0.78}(Na_{0.02}Ca_{0.01})(Al_{1.46}Mg_{0.27}Fe_{0.27})Si_{3.38}Al_{0.62}O_{10}(OH)_2$, with trace quantities of quartz (detectable by XRD) and potassium feldspar crystals (SEM/EDS imaging). Glycolation and re-analysis with XRD showed no indication of expanding clays (i.e., smectite) at the resolution of the method, consistent with prior characterization of this material (Gailhanou et al., 2012; Hower and Mowatt, 1966). The surface area of the unreacted illite grains was 30.7 ±2 m^2 g^{-1}. Experiments conducted at pH > 6 showed no detectable change in measured surface area, while products from more acidic experiments decreased by 2-5x.

SEM imaging of experimental products from high-temperature acid-pH experiments showed intense alteration of the illite grains (in some cases even near-total transformation) into masses of smaller (~2μm diameter) tabular crystals. These newly formed precipitates showed diffraction patterns consistent with boehmite (γ-AlO(OH)) when measured in bulk, while individual crystals analyzed by TEM were determined to be diaspore (α-AlO(OH)). No Si-bearing precipitates or other reaction products were noted by any analysis technique. Due to the identification of these secondary precipitates, calculated final illite mass and initial illite surface area value were used in all illite dissolution rate derivations. More detail is provided in Smith and Carroll (2015) and a forthcoming publication in preparation.

2.1.3 Biotite

An Mg-rich variety of biotite (phlogopite) was provided courtesy of Dr. Young-Shin Jun of Washington University. Individual biotite sheets were first shredded in a coffee grinder before milling and sieving. The composition of this material as determined by microprobe was $K_{0.94}(Na_{0.05})(Mg_{2.64}Fe_{0.17}Al_{0.12}Ti_{0.04})Si_{2.88}Al_{1.12}O_{10}(OH)_2$, with no impurities noted by either XRD or SEM imaging methods. This composition is generally similar to that determined by Shao et al. (2011) on the same material. Specific surface area of unreacted biotite was 10.7 m^2 g^{-1}, with no apparent changes after reaction. No reaction products (secondary precipitates) have yet been observed by XRD although TEM analyses have not yet been completed.

2.2 Experimental Methods

All kinetic experiments were conducted by passing 0.05m NaCl solutions at the same fixed flowrate (0.5 mL min-1) through constantly stirred single-pass reactors (e.g., Dove and Crerar, 1990) containing 0.5-1.0g of 150-250 μm mineral grains. The use of flow-through reactors, as opposed to batch systems, allows effluent fluid compositions to adjust to apparent steady-state levels while maintaining constant inflowing fluid composition (ensuring a constant Gibbs free energy of reaction). Concentrated HCl and NaOH were used to adjust influent solution pH in order to achieve desired solution pH values at elevated temperature. We note that due to changes in the dissociation constant of water, neutral pH shifts to higher pH values (5.5-6.5) over this 100-280°C temperature range. A back-pressure regulator was employed to maintain fluid pressures well above boiling point and ensure single-phase flow. Experiments were conducted for durations of 3-7 days. All wetted reactor parts were constructed of titanium, C-276 allow, or PEEK, to reduce chemical interactions.

Aqueous samples were collected at the back-pressure port and analyzed for major and trace elements of interest by inductively-coupled plasma mass spectrometry, and solution pH measurements were made at room temperature. The geochemical code EQ3/6 and the updated *data0.ymp.R5* database (Wolery, 1992; Johnson et al., 1992) were used to calculate ion speciation, correct measured pH for

elevated temperature, and estimate fluid-mineral saturation indices (log IAP/K_{eq}, where IAP is the ion activity product and K_{eq} is the solubility product for a given reaction). Apparent steady-state concentrations, C, of analyte i (most commonly silica) were used to derive dissolution rates, R [mol m^{-2} s^{-1}], according to

$$R = \frac{C_i \cdot \upsilon \cdot \sigma_{i,m}}{m_m \cdot SSA_m} \quad (1)$$

where υ is the flowrate, m_m is the mass [g] of the solid mineral m, and SSA_m is the measured N_2-BET specific surface area of mineral m [m^2 g^{-1}] prior to reaction. For most experiments the change in mineral mass, m_m, over the course of the experiment was minimal and made no impact to the final rate calculation, with the exception of illite dissolution at acidic pH where dissolution rate proceeded rapidly and large changes to this quantity were observed. In these cases, final m_m values were calculated by integrating the total mass of dissolved silica from each experiment and converting that value to a final mass [g] using an estimated illite formula weight of 399 g mol^{-1}.

Surface area-corrected rate values were modeled with an empirical form of kinetic rate expression relating rate magnitude to temperature and chemical activity:

$$R_{dissolution} = \left[\left(A_A \cdot e^{-E_A/RT} \cdot a_{H+}^{n} \right) + \left(A_N \cdot e^{-E_N/RT} \right) + \left(A_B \cdot e^{-E_B/RT} \cdot a_{OH-}^{m} \right) \right] \cdot f(\Delta G_r) \quad (2)$$

where A_i represents pre-exponential constants [mol m^{-2} s^{-1}] and E_i represents activation energies [kJ mol^{-1}] for each of the pH-mediated dissolution regimes (*A*cid, *N*eutral, and *B*asic/alkaline); n and m represent orders of reaction with respect to hydronium and hydroxide activities (a_{H+}, a_{OH-}, [molal]); T is temperature [K]; R is the gas constant [J K^{-1} mol^{-1}]; and $f(\Delta G_r)$ represents some dependence on the Gibbs free energy of reaction. Groups of parameters describing a single pH-mediated mechanism have been shown to be highly correlated (e.g., Smith and Carroll, 2016), and thus Arrhenius fits were utilized to generate fixed E_i values so that other parameters could be optimized with greater confidence. Final rate equations were produced through a combination of software-aided parameter optimization (PEST; Doherty, 2005) and graphical fitting. Where available, the rate data from these studies were supplemented with published rates from similar pH ranges to produce kinetic dissolution rate equations applicable over the widest range of potential geothermal conditions.

3. RESULTS AND DISCUSSION

Results from chlorite and illite dissolution have been presented and discussed previously (Smith and Carroll, 2015, 2016; Smith et al., 2013) and will be only briefly summarized here for purposes of comparison. Newly collected biotite dissolution rates from 100-280°C will be discussed in more detail.

3.1 Congruency of dissolution

Comparison of elemental release rates from each set of mineral dissolution experiments provides valuable information about how and to what extent portions of the crystal structure dissolve (e.g., interlayer versus tetrahedral and octahedral ions), and also indicates which elements are best suited to describe the overall dissolution rate. The ratios of steady-state aluminum, magnesium, and potassium release rates relative to dissolved silica from biotite dissolution experiments are shown in Figure 1 versus solution pH. In Figure 1a, Al:Si ratios approach that of the unreacted material (signifying congruent dissolution) only for pH > 6-7, with Al:Si decreasing by several orders of magnitude at lower pH values. This behavior is similar to that observed for the other sheet silicates, with Al:Si released congruently at pH > 7 and at pH >8 for illite. Previous researchers studying a related sheet silicate, muscovite, hypothesized that an Al-bearing phase may have been precipitating and affecting Al concentrations (e.g., Kalinowski and Schweda, 1996; Knauss and Wolery, 1989; Lin and Clemency, 1981). Previous low-temperature work on illite dissolution at acid pH did not identify secondary Al-precipitates but an aluminum oxy-hydroxide phase (AlO(OH)(s)) was noted in acidic illite experiments in our study (see section 2.1.2). Neither aluminum hydroxides or aluminosilicate precipitates have been observed as a result of reaction of the Mg-Al-sheet silicates (chlorite, biotite). Aluminum is distributed in both tetrahedral and octahedral sites in these minerals, with the fraction in tetrahedral sites decreasing as illite > chlorite >> biotite.

During chlorite and biotite dissolution, Mg:Si ratios are close to stoichiometric levels of the unreacted material for pH < 5.5-6, as shown in Figure 1b. Above this pH limit, Mg:Si ratios decrease with increasing pH, albeit to a lesser extent that was noted for aluminum. For the case of illite, where Mg is present at roughly 10% of the molar fraction in chlorite or biotite, Mg:Si ratios are uniformly several orders of magnitude lower than the initial ratios in unreacted illite across the pH range investigated. For both chlorite and biotite, the magnitude of the decrease in Al:Si and Mg:Si release ratios is correlated with increasing temperature. Magnesium is held primarily in octahedral coordination in these three minerals.

K:Si release ratios relative to silica from biotite experiments are shown in Figure 1c and display strongly preferential release of potassium relative to silica over most of the pH range of the experiments, assuming conservative dissolved silica levels. This behavior stands in contrast to the near-stoichiometric release of potassium from illite dissolution experiments over pH 2.5-9 (data not shown). Potassium is found primarily in interlayer sites between repeating sequences of T-O-T layers in both minerals. It is important to note that background solution levels of Na+ were kept similar in all experiments, and thus cation substitution seems an unlikely explanation for these different trends.

From these ratios and those from previous chlorite and illite work (Smith and Carroll, 2015; 2016), it is clear that neither aluminum nor magnesium provides a confident measure of mineral dissolution over the entire pH range of interest. Potassium may be an acceptable element for use in rate derivation for illite, but its use to describe biotite reaction will overestimate dissolution rates by more than an order of magnitude. Based on these results and on the current lack of observable silica-bearing reaction products, we use measured dissolved silica concentrations to derive kinetic dissolution rate values for these sheet silicates.

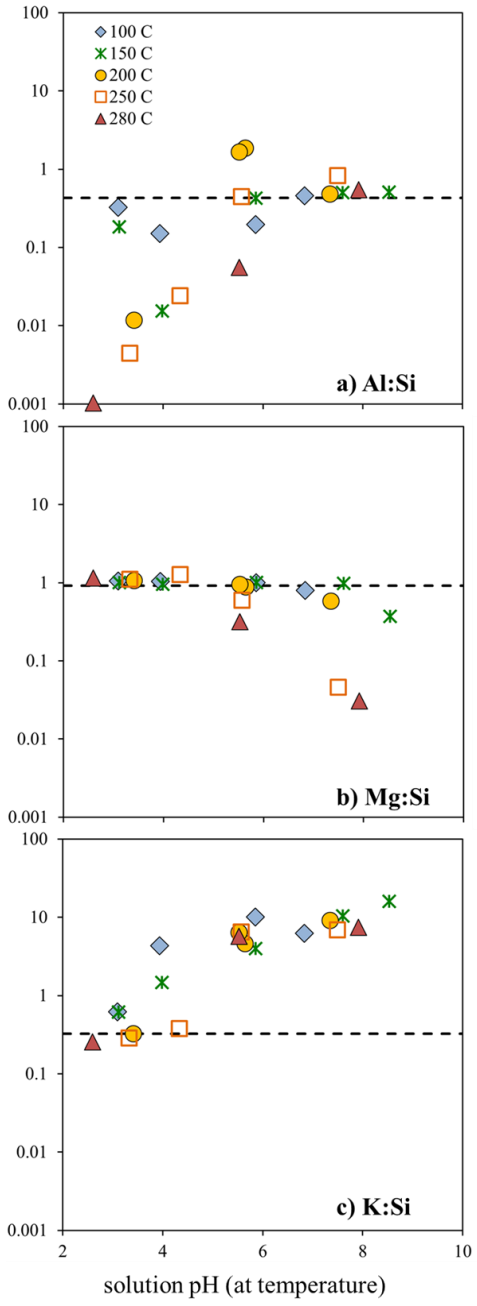

Figure 1: Ratios of elemental release rates relative to dissolved silica, versus solution pH at temperature from biotite experiments; A) Al:Si, B) Mg:Si, and C) K:Si. Heavy dashed lines denote the ratio in the unreacted material. Note the logarithmic scale of the y-axes.

3.2 Dissolution rates, temperature, and solution pH

Dissolution rates of chlorite, illite, and biotite, collected over temperatures of 100-280°C and a pH range of 3-9, as well as fitted rate equations are shown in Figure 2. More detail concerning the derivation of chlorite and illite rates and rate equations may be found in Smith and Carroll (2015; 2016). In addition, new silica-derived biotite dissolution rates are shown in Table 1.

At lower temperatures, chlorite and illite rates plotted against solution pH show a subdued parabolic relationship with the fastest acidic rates and the slowest neutral pH rates differing by less than an order of magnitude, but above 200°C rates tend to increase more strongly for a given drop in solution pH. Biotite rates, in contrast, increase by about twice as much at a given temperature between neutral and acidic pH conditions. At a given pH, however, chlorite and biotite dissolution rates (Figures 2a,c) show much less variation with temperature compared to illite (Figure 2b), and dissolution rates from all three minerals tend to lose temperature dependence at 200°C and above for a given pH.

For both chlorite and biotite (Figures 2a,c), rates do not appear to increase (and in some cases decrease, see increasing fluid saturation indices with increasing pH, Smith and Carroll, 2016 and Table 1) in magnitude as pH increases into the alkaline region. We note that solution pH measured at 25°C shifts to lower values when recalculated at *in situ* temperature (100-280°C) as a result of the change in neutral pH at higher temperatures (see section 2.2). It is possible that these experiments are simply not sufficiently alkaline to yet see increases in rates (i.e., the parabolic rate-pH relationship); however, it is also possible that fluid saturation with respect to chlorite and biotite may be influencing the dissolution rate at pH > 8. Fewer reliable chlorite and biotite rate data were collected at higher pH both as a consequence of pump damage caused by highly alkaline 25°C influent solutions and because several experiments at these pH levels were terminated early due to pressure buildup within the experimental reactors. It should be noted that illite (K-Al-silicate, lacking Mg) rates do show significant increases with increased pH at 100 and 150°C.

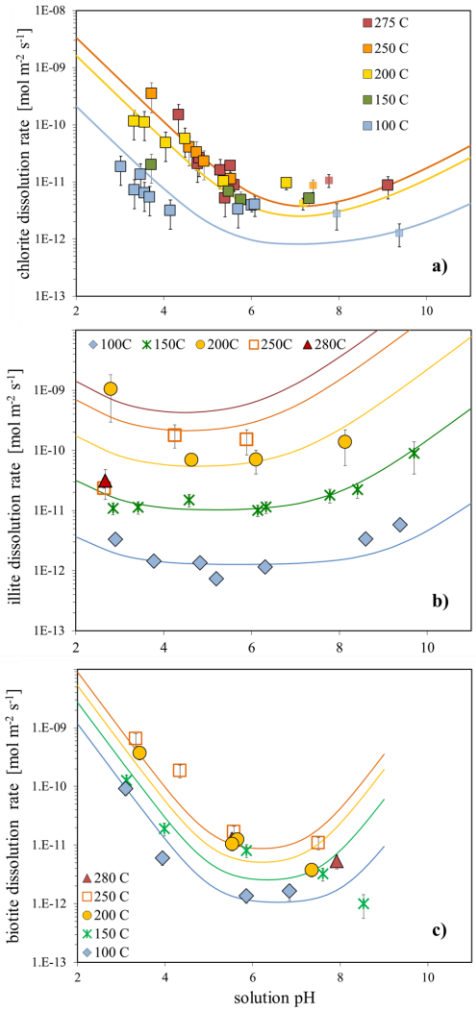

Figure 2: Dissolution rates of a) chlorite, b) illite, and c) biotite versus solution pH at temperatures of 100, 150, 200, 250, and 280°C. Figure 2a adapted from Smith and Carroll, 2016. Kinetic rate models (equations 3-5) are shown as solid lines, and represent far-from-equilibrium (i.e., $f(\Delta G_r) \approx 1$) conditions.

temperature °C	solution pH	dissolution rate mol m^{-2} s^{-1}	biotite/phlogopite log IAP/K_{eq}	ΔG_r kJ mol^{-1}
100	3.1	$9.2(\pm2)\cdot10^{-11}$	-31	-219
100	3.9	$6.0(\pm1)\cdot10^{-12}$	-32	-229
100	5.9	$1.4(\pm0.3)\cdot10^{-12}$	-22	-161
100	6.8	$1.6(\pm0.5)\cdot10^{-12}$	-14	-103
150	3.1	$1.3(\pm0.3)\cdot10^{-10}$	-21	-172
150	4.0	$1.9(\pm0.5)\cdot10^{-11}$	-23	-186
150	5.9	$8.1(\pm2)\cdot10^{-12}$	-14	-115
150	7.6	$3.2(\pm0.8)\cdot10^{-12}$	-6.6	-53
150	8.5	$1.0(\pm0.4)\cdot10^{-12}$	-4.9	-39
200	3.4	$3.7(\pm0.9)\cdot10^{-10}$	-18	-163
200	5.5	$1.0(\pm0.2)\cdot10^{-11}$	-13	-120
200	5.6	$1.2(\pm0.3)\cdot10^{-11}$	-12	-106
200	7.4	$3.8(\pm0.9)\cdot10^{-12}$	-4.2	-38
250	3.3	$6.5(\pm2)\cdot10^{-10}$	-15	-154
250	4.3	$1.8(\pm0.5)\cdot10^{-10}$	-8.8	-88
250	5.6	$1.7(\pm0.4)\cdot10^{-12}$	-10	-105
250	7.5	$1.1(\pm0.3)\cdot10^{-11}$	-5.1	-51
280	5.5	$1.3(\pm0.3)\cdot10^{-11}$	-11	-118
280	7.9	$5.3(\pm0.3)\cdot10^{-12}$	-4.2	-44

Table 2: Biotite experimental conditions, dissolution rates, modeled fluid-biotite saturation indices (log IAP/K_{eq}) and Gibbs free energies of reaction (ΔG_r).

3.3 Effect of fluid saturation

Figure 3 shows modeled fluid-mineral saturation indices from 150°C experiments plotted against solution pH. Over a pH range of ~3-9, fluid saturation indices continuously increase, approaching or in some cases surpassing equilibrium (log IAP/K_{eq} = 1) with respect to chlorite and biotite as solution pH increases. Fluid-illite saturation indices reach a maximum at circumneutral pH and then decrease significantly with further increases in pH. These trends indicate the importance of both pH and saturation effects, but these datasets cannot be used to differentiate between the two effects. A statistically significant number of rates measured at elevated temperature and fixed pH/variable ΔG_r (or vice versa) will be needed to distinguish the impact of these two mechanisms, similar to the efforts of Nagy and Lasaga (1992), Cama et al. (2000), or Zhang et al. (2015). In the current absence of higher-temperature studies to sufficiently constrain an appropriate form of reaction affinity term, $f(\Delta G_r)$, and as discussed in Smith and Carroll (2016), we propose to use a simple form (see equations (3-5), below).

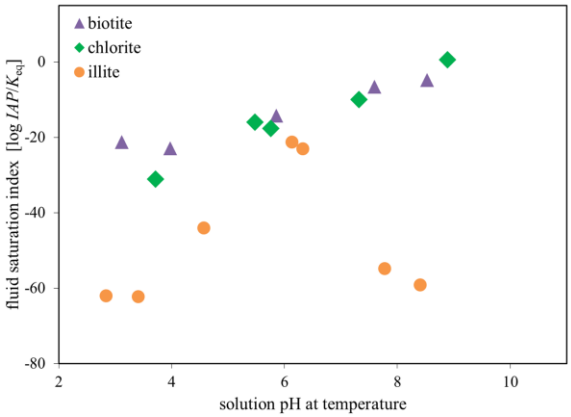

Figure 3: Modeled mineral-fluid saturation indices (log IAP/K_{eq} values) versus solution pH for experiments conducted at 150°C.

3.4 Derivation of rate equations

Because the empirical rate model used in this study (equation (2) contains a large number of parameters, some of which are strongly correlated, efforts can be made to determine activation energies, E_i, through a graphical approach (i.e., an Arrhenius treatment of apparent natural log rates versus inverse temperature). Estimating activation energies in this manner, and n, m values if possible, decreases the number of fitted parameters but does require the assumption that no other rate dependences have significant effects on rate values.

Arrhenius treatments of silica-, potassium-, magnesium-, and aluminum-derived rates from biotite experiments are shown in Figure 4, with best-fit slopes to the silica data shown as dashed lines. At acid pH (Figure 4a), K/Mg/Si rate values plot along a similar trend while Al rates decrease, similar to the behavior in Figure 1a. As pH increases, K rates increase due to preferential release and Mg/Al rates are nonlinearly correlated with pH (Figure 4b). At alkaline conditions, Mg rates deviate from the trend shown by Si/Al data. Chlorite (to a lesser extent) and illite rates showed similar behavior at acid pH levels. It is interesting to note that acid illite dissolution is accompanied by AlO(OH) precipitation which accounts well for the aluminum deviation, but no Al-bearing secondary precipitates could be found in the chlorite reaction products (Smith and Carroll, 2016). Si-derived activation energies for chlorite are highest in the acid pH regime and continually decrease as pH increases, while K/Al/Si rates from the Mg-free illite all approach congruency and yield increasing activation energies with increasing pH (data not shown).

The fitted rate equations (fits shown as solid lines in Figure 3) are provided below. The chlorite rate equation was developed using data from our study and from the work of Zhang et al. (2015; 100°C), Black and Haese (2014; 50-120°C), Lowson et al. (2005, 2007; 25-95°C), and Brandt et al. (2003; 25°C), and is discussed in more detail in Smith and Carroll (2016):

$$R_{chlorite} = \left[\left(1\cdot10^{-4}\cdot e^{-30/RT}\cdot a_{H+}^{0.74}\right)+\left(4.7\cdot10^{-11}\cdot e^{-13/RT}\right)+\left(1.5\cdot10^{-9}\cdot e^{-15/RT}\cdot a_{OH-}^{0.43}\right)\right]\cdot\left(1-e^{\Delta G_r/RT}\right) \quad (3)$$

The illite equation given here and in Figure 3b was developed using data from our study, first discussed in Smith and Carroll (2015), as well as 25°C data from Köhler et al. (2003) and Bibi et al. (2011).

$$R_{illite} = \left[\left(5\cdot10^{-3}\cdot e^{-58/RT}\cdot a_{H+}^{0.6}\right)+\left(4.5\cdot10^{-5}\cdot e^{-54/RT}\right)+\left(3.5\cdot e^{-77/RT}\cdot a_{OH-}^{0.55}\right)\right]\cdot\left(1-e^{\Delta G_r/RT}\right) \quad (4)$$

A kinetic rate to describe biotite data from our study is provided here and shown in Figure 3c. It should be noted that this rate equation is applicable only over 100-280C and has been developed using only the higher-temperature rates given in Table 1. Future work to incorporate existing biotite rate datasets (e.g., Kalinowski and Schweda, 1996) may require revision to some fitted parameter values:

$$R_{biotite} = \left[\left(1.4\cdot10^{-4}\cdot e^{-22/RT}\cdot a_{H+}^{1.0}\right)+\left(1.2\cdot10^{-9}\cdot e^{-22/RT}\right)+\left(1\cdot10^{-6}A_B\cdot e^{-13/RT}\cdot a_{OH-}^{1.0}\right)\right]\cdot\left(1-e^{\Delta G_r/RT}\right) \quad (5)$$

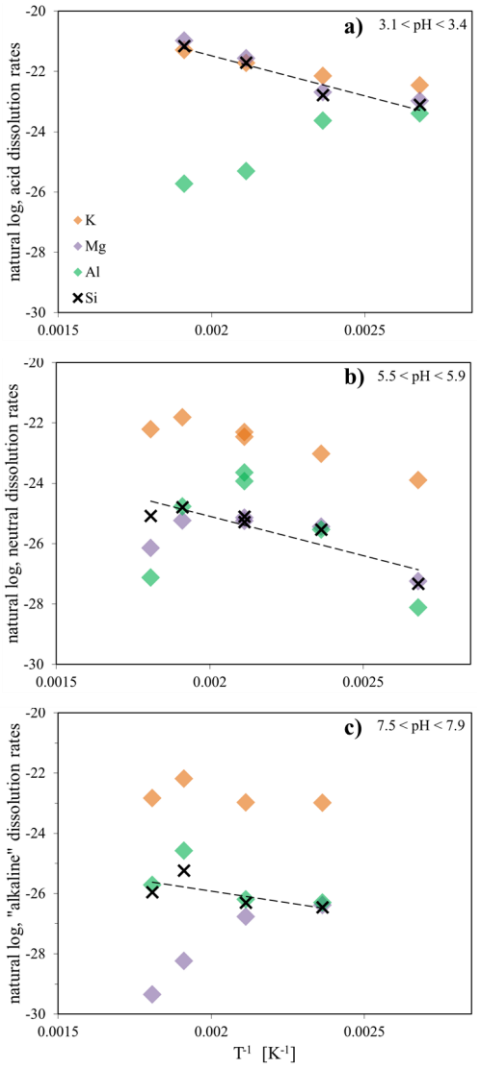

Figure 4: Natural log biotite dissolution rates versus inverse temperature, K^{-1}, for a) acidic, b) circumneutral, and c) the most alkaline conditions. Rates shown here are estimated from silica (black x), potassium (orange symbols), aluminum (green symbols), and magnesium (purple symbols) concentrations. Dashed black lines represent best-fit slopes to silica data only and correspond to apparent activation energies of 22, 22, and 13 kJ mol^{-1}.

4. CONCLUSIONS

Kinetic dissolution experiments with three common sheet silicate minerals (chlorite, Mg-Al-silicate; illite, K-Al-silicate; and biotite, K-Mg-Al-silicate) were conducted over a temperature range of 100-280 °C and a pH range of 3-9. Previously published rate equations derived primarily from 25 °C data both over- (in the case of chlorite; Lowson et al., 2005; Palandri and Kharaka, 2004) and under-predict (in the case of illite; Köhler et al., 2003) rates by orders of magnitude at higher-temperature geothermal conditions. Our experiments show that for a given pH, illite is the most reactive of the three sheet silicates with rates increasing by over 1000 times from 100-280 °C over a 3-4 day timescale, compared to a 10-50fold increase in chlorite and biotite rates over the same time and temperature range. We find that illite dissolution under acid conditions is accompanied by rapid co-precipitation of aluminum oxy-hydroxide solids, with no secondary precipitation noted under neutral or alkaline conditions. In comparison, chlorite and biotite experiments showed no evidence of secondary precipitates (although biotite reaction product analysis is ongoing), and dissolution rates of these two minerals showed little variability at pH ≥ 5 as solutions approached equilibrium with magnesium-hydroxide phases. We present kinetic rate equations that should be useful for prediction of the long-potential term impacts of geochemical alteration on reservoir permeability.

This work performed under the auspices of the U.S. Department of Energy by Lawrence Livermore National Laboratory under Contract DE-AC52-07NA27344.

REFERENCES

Bibi, I., Singh, B., and Silvester, E.: (2011) Dissolution of illite in saline-acidic solutions at 25°C, *Geochimica et Cosmochimica Acta*, **75**, (2011), 3237-3249.

Black, J.R., and Haese, R.R.: Chlorite dissolution rates under CO_2 saturated conditions from 50 to 120°C and 120 to 200 bar CO_2, *Geochimica et Cosmochimica Acta*, **125**, (2014), 225-240.

Brandt, F., Bosbach, D., Krawczyk-Bärsch, E., Arnold, T., and Bernhard G.: Chlorite dissolution in the acid pH-range: A combined microscopic and macroscopic approach, *Geochimica et Cosmochimica Acta*, **67**, (2003), 1451-1461.

Cama, J., Ganor J., Ayora C., and Lasaga A.C.: Smectite dissolution kinetics at 80 °C and pH 8.8., *Geochimica et Cosmochimica Acta*, **64**, (2000), 2701-2727.

Detwiler, R.L., Glass, R.J., and Bourcier W.L.: Experimental observations of fracture dissolution: the role of Peclet number on evolving fracture aperture. *Geophysical Research Letters*, **30**, (2003), (12).

Doherty, J.: PEST: Software for model-independent parameter estimation, Watermark Numerical Computing, Australia, (2005). http://www.pesthomepage.org, accessed January 2016.

Durham, W.B., Bourcier, W.L., and Burton, E.A.: (2001) Direct observation of reactive flow in a single fracture. *Water Resources Research*, **37**, (2001), 1-12.

Ellis, B.R., Fitts, J.P., Bromhal, G.S., McIntyre, D.L., Tappero, R., and Peters, C.A.: Dissolution-driven permeability reduction of a fractured carbonate Caprock, *Environmental Engineering Science*, **30**, (2013), 187-193.

Gailhanou, H., Blanc, P., Rogez, J., Mikaelian, G., Kawaji, H., Olives, J., Amouric, M., Denoyel, R., Bourrelly, S., Montouillout, V., Viellard, P., Fialips, C.I., Michau, N., and Gaucher, E.C.: Thermodynamic properties of illite, smectite and beidellite by calorimetric methods: Enthalpies of formation, heat capcities, entropies and Gibbs free energies of formation, *Geochimica et Cosmochimica Acta*, **89**, (2012), 279-391.

Hower, J., and Mowatt, T.C.: The mineralogy of illites and mixed-layer illite/montmorillonites, *American Mineralogist*, **51**, (1966), 825-854.

Johnson, J.W., Oelkers, E.H., and Helgeson, H.C.: SUPCRT92: A software package for calculating the standard molal thermodynamic properties of minerals, gases, aqueous species, and reaction from 1 to 5000 bar and 0 to 1000°C. *Computational Geosciences*, **18**, (1992), 899-947.

Kalinowski, B.E., and Schweda, P.: Kinetics of muscovite, phlogopite, and biotite dissolution and alteration at pH 104, room temperature, *Geochimica et Cosmochimica Acta*, **60**, (1996), 367-385.

Köhler, S.J., Dufaud, F., and Oelkers, E.H.: An experimental study of illite dissolution kinetics as a function of pH from 1.4 to 12.4 and temperature from 5 to 50°C, *Geochimica et Cosmochimica Acta*, **67**, (2003), 3583-3594.

Knauss, K.G., and Wolery, T.J.: Muscovite dissolution kinetics as a function of pH and time at 7 °C, *Geochimica et Cosmochimica Acta*, **53**, (1989), 1493-1501.

Lin, F.-C., and Clemency, C.V.: The kinetics of dissolution of muscovites at 25°C and 1 atm CO_2 partial pressure, *Geochimica et Cosmochimica Acta*, **45**, (1981), 571-576.

Lowson, R.T., Comarmond, M.-C.J., Rajaratnam, G., Brown, P.L.: The kinetics of the dissolution of chlorite as a function of pH at 25C, *Geochimica et Cosmochimica Acta*, **69**, (2005), 1687-1699.

Lowson, R.T., Brown, P.L.Comarmond, M.-C.J., Rajaratnam, G.: The kinetics of chlorite dissolution, *Geochimica et Cosmochimica Acta*, **71**, (2007), 1431-1447.

Lutz, S.J., Hickman, D., Davatzes, N., Zemach, E., Drakos, P., Robertson-Tait, A.: Rock mechanical testing and petrological analysis in support of well stimulation activities at the Desert Peak Geothermal Field, Nevada, Proceedings, 35th Workshop on Geothermal Reservoir Engineering, Stanford University, Stanford, CA (2010).

Moore, D.E., Lockner, D.A., and Byerlee, J.D.: Reduction of permeability in granite at elevated temperatures, *Science*, **265**, (1992), 1558-1561.

Nagy, K.L., and Lasaga, A.C.: Dissolution and precipitation kinetics of gibbsite at 80°C and pH 3: the dependence on solution saturation state, *Geochimica et Cosmochimica Acta*, **56**, (1992), 3093-3111.

Palandri, J.L., and Kharaka, Y.K.: A compilation of rate parameters of water-mineral interaction kinetics for application to geochemical modeling, U.S. Geological Survey Open File Report 2004-1068 (2004).

Polak, A., Elsworth, D., Liu, J., and Grader, A.S.: Spontaneous switching of permeability changes in a limestone fracture with net dissolution, *Water Resources Research*, **40**, (2004), W03502.

Polak, A., Elsworth, D., Yasuhara, H., Grader, A.S. and Halleck, P.M.: Permeability reduction of a natural fracture under net dissolution by hydrothermal fluids, *Geophysical Research Letters*, **30**, (2003), 20.

Shao, H., Ray, J.R., and Jun, Y-S.: Effects of salinity and the extent of water on supercritical CO_2-induced phlogopite dissolution and secondary mineral formation, *Environmental Science & Technology*, **45**, (2011), 1737-1743.

Smith, M.M., Walsh, S.D.C., McNab, W.W., and Carroll, S.A.: Experimental investigation of brine-CO2 flow througha natural fracture: permeability increases with concurrent dissolution/reprecipitation reactions, *Proceedings*, 38th Workshop on Geothermal Reservoir Engineering, Stanford University, Stanford, CA (2013).

Smith, M.M., Wolery, T.J., and Carroll, S.A.: Kinetics of chlorite dissolution at elevated temperatures and CO_2 conditions, *Chemical Geology*, **347**, (2013), 1-8.

Smith, M.M., Hao, Y., Mason, H.M., and Carroll, S.A.: (2014) Experiments and modeling of variably permeable carbonate reservoir samples in contact with CO2-acidified brines, *Energy Procedia*, **63**, 3126-3137.

Smith, M.M. and Carroll, S.A.: High-temperature illite dissolution kinetics, *Proceedings*, 40th Workshop on Geothermal Reservoir Engineering, Stanford University, Stanford, CA (2015).

Smith, M.M. and Carroll, S.A.: Chlorite dissolution kinetics from pH 3 to 10 and temperature to 275C, *Chemical Geology*, **421**, (2016), 55-64.

Wolery,T.J.: EQ3/6, a software package for geochemical modeling of aqueous systems, Lawrence Livermore National Laboratory Report UCRL MA-110662 PT 1 (1992).

Yasuhara H., and Elsworth, D.: Compaction of a rock fracture moderated by competing roles of stress compaction and pressure solution, *Applied Geochemistry*, **26**, (2004), 204-2088.

Yasuhara, H., Polak, A., Mitani, Y., Grader, A.S., Halleck, P.M., and Elsworth, D.: Evolution of fracture permeability through fluid-rock reaction at hydrothermal conditions, *Earth and Planetary Science Letters*, **244**, (2006, 186-2000.

Zavarin, M., Powell, B.A., Bourbin, M., Zhao, P., and Kersting, A.B.: Np(V) and Pu(V) ion exchange and surface-mediated reduction mechanisms on montmorillonite, *Environmental Science and Technology*, **46**, (2012), 2692-2698.

Zhang, S., Yang, L., DePaolo, D.J., and Steefel, C.I.: Chemical affinity and pH effects on chlorite dissolution kinetics under geological CO_2 sequestration related conditions, *Chemical Geology*, **396**, (2015), 208-217.